



Study on the organization and properties of Ti–6Al–4 V fabricated by laser powder bed fusion based on the thickness of the gradient layer

Peng Wang^{1,2} · Dongju Chen^{1,2} · Jinwei Fan^{1,2} · Gang Li^{1,2}

Received: 17 October 2022 / Accepted: 13 March 2023 / Published online: 20 March 2023
© The Author(s), under exclusive licence to Springer-Verlag London Ltd., part of Springer Nature 2023

Abstract

Intelligent additive manufacturing is the future direction, and changing parameters during manufacturing process is an effective measure to adjust the quality of parts. In this study, the stability behavior of the manufacturing process under three process strategies, low layer thickness fabrication (LLTF), high layer thickness fabrication based on the interval of the powder layer thickness (IPLT), and changing of layer thickness strategy (CLTS), was comparatively investigated. Multilayer experiments and mechanical properties experiments were performed during laser powder bed fusion, and the correlation between manufacturing quality and powder layer thickness was compared. By optimizing the process parameters, the surface quality of CLTS is similar to that of LLTF, and the value of minimum surface roughness can be between 22 and 23 μm . Only balling effect due to spattering and a small amount of porosity were found in the cross-section of CLTS. The relative density of most of the fabricated parts is higher than 99%, and the highest relative density is up to 99.99%. IPLT has longer and thicker martensite than LLTF, and the β -grain of CLTS is also coarser than LLTF. The tensile properties of CLTS are similar to those of LLTF, and the ultimate tensile strength, yield strength and elongation of CLTS are 1205 MPa, 1107 MPa and 6.8%, respectively. Due to the anisotropy of the LPBF, the horizontally constructed Ti–6Al–4 V specimens yielded higher strengths, while the vertically constructed specimens obtained better elongation. The fracture of the part is characterized by a mixture of brittle fracture, ductile fracture and quasi-dissociative fracture. The surface quality, relative density and mechanical properties of CLTS are similar to those of LLTF, while the forming efficiency is much higher than that of LLTF, which can reach 7.35 mm^3/s .

Keywords Laser powder bed fusion · Ti–6Al–4 V · Changing of layer thickness strategy · Stability behavior · Microstructure and mechanical properties

1 Introduction

Laser powder bed fusion (LPBF), one of the most important additive manufacturing (AM) technologies, has gained much attention for its unique advantages in near-net forming of metal parts with complex geometries. Based on the

principle of powder bed fusion, a high-energy laser beam is used to melt the metal powder layer by layer and point by point to fabricate the parts according to the pre-designed 3D model data [1, 2]. Since the laser beam and metal powder are used as manufacturing tools to quickly and economically manufacture complex-shaped parts, the tools and fixtures are eliminated, such that the processing cycle is significantly shortened [3, 4]. LPBF allows the preparation of complex metal parts with low surface roughness, high relative density and excellent mechanical properties [5, 6]. Titanium alloy is an important non-ferrous metal with the advantages of low density, low coefficient of thermal expansion, excellent corrosion resistance, high specific strength, outstanding resistance to low temperature brittleness, fine weldability, non-toxic and non-magnetic. Ti–6Al–4 V is the most classical

✉ Dongju Chen
djchen@bjut.edu.cn

¹ Mechanical Industry Key Laboratory of Heavy Machine Tool Digital Design and Testing, Faculty of Materials and Manufacturing, Beijing University of Technology, Ping Leyuan 100#, Chaoyang District, Beijing 100124, China

² Beijing Key Laboratory of Advanced Manufacturing Technology, Faculty of Materials and Manufacturing, Beijing University of Technology, Beijing 100124, China

titanium alloy that has been widely used in aerospace [7] and biomedical implants [8, 9].

The fabricating efficiency of LPBF can be improved by increasing the scanning speed and increasing the layer thickness [10]. Ahn found that layer thickness had a greater effect on fabrication time than scanning speed and that increasing the layer thickness by about 1.6 times could reduce fabrication time by up to 40% [11]. In addition, Ma et al. prepared 1Cr18Ni9Ti parts using a high layer thickness of 150 μm , and the fabricating efficiency was improved by more than 10 times [12]. Wang et al. increased the layer thickness to 150 μm to obtain the fabricating efficiency as high as $12\text{mm}^3/\text{s}$ [13]. Liu et al. increased the layer thickness to 200 μm , the fabricating efficiency could be increased to $12.4\text{mm}^3/\text{s}$ and the heat-treated could achieve excellent mechanical properties [14]. However, the increase in layer thickness will lead to a decrease in the mechanical performance. Savalani et al. found smoother and flatter surfaces for lower layer thicknesses [15]. Wang et al. showed that progressively thicker layers were responsible for the deterioration of surface quality in multilayer experiments [16]. Nguyen et al. showed that the lower layer thickness, the higher the dimensional accuracy [17]. Greco et al. showed that due to the limited depth of laser energy into the powder bed, the layer thickness leads to a decrease in relative density and microhardness [18]. In addition, the layer thickness affects the microstructure of LPBF fabricated parts [19]. The multi-laser beam stitching molding systems are equipped with multiple scanning systems, so the size and efficiency that can be molded while maintaining the existing forming accuracy will be substantially increased [20]. However, these approaches involve significant research and development and typically lead to more expensive LPBF machines [21].

Assembly-free structures may include many different types of structures at the same time, and the use of different process parameters for different structures will ensure high quality formation of the part. The process parameters and layer thicknesses in the LPBF process are non-variable, which can easily lead to stress concentrations and mismatches between productivity and forming quality. The development and utilization of more advanced hierarchical software will be more conducive to the improvement of efficiency and accuracy. Appropriate materials are used at suitable locations, and suitable layer thicknesses are used for different materials. For these reasons, this paper focuses on a new method to achieve high quality and high efficient LPBF fabricating process. Formanoir et al. confirmed the feasibility of using different layer thicknesses in LPBF [21]. The study demonstrates parts can be additively built using multiple layer thickness regions with consistent ultimate tensile strength (1110–1135 MPa) and varying penalties to ductility. In this paper, we propose a new process method with changing of layer thickness strategy (CLTS), the application

of which can greatly release the freedom of LPBF design and manufacturing. CLTS is a fabricating strategy that uses different layer thicknesses in the fabricating process. A high laser energy density parameter is used to melt and form a high thickness powder layer, and then a low laser energy density parameter is used to melt and form a thin thickness powder layer, to achieve alternating high and thin layer thicknesses. Thin layer thickness is used for slicing and layering, and the powder is laser scanned after a certain number of layers are spaced to complete the IPLT strategy. For example, a layering thickness of 50 μm is used, and the first and second layers are used as spacer layers without melting the powder, and the third layer is melted with a laser beam, thus achieving the purpose of interlayer strategy, while the actual layer thickness is 150 μm . Excellent mechanical properties (tensile strength, yield strength, elongation and microhardness) can be obtained by implementing the CLTS strategy and adjusting the process parameters (laser power and exposure time, etc.). The optimal mechanical properties and optimal microhardness obtained in this study are comparable to those of low layer thickness fabrication. The advantage of using CLTS is that the mechanical properties can be guaranteed while improving the fabricating efficiency, and this fabricating strategy will greatly improve the application prospects of LPBF.

Given the close correlation between process parameters and microstructure, the use of different machining conditions in CLTS may lead to the formation of unique microstructures that affect mechanical properties. Different laser powers and scanning speeds lead to different α' phases. LPBF-produced Ti–6Al–4 V alloy at relatively low laser power and scanning velocity results in coarsening α' grains and at relatively high laser power and scanning velocity results in fine α' laths [22]. Xu et al. [23] found that changing the layer thickness, energy density and laser focus offset distance can effectively regulate the α' martensite content in the Ti–6Al–4 V alloy tissue and achieve in situ decomposition of α' martensite to obtain a tissue containing only $(\alpha + \beta)$ lamellae. The microstructure of Ti–6Al–4 V after heat treatment usually contains $(\alpha + \beta)$ lamellar tissue within the initial state β columnar crystal. The complex thermal history in CLTS affects the fine microstructure of Ti–6Al–4 V parts, and to validate the use of CLTS in critical industrial applications, it is important to determine the extent to which this strategy affects the LPBF Ti–6Al–4 V parts' microstructure and mechanical properties. The effects of process parameters on the surface properties, cross-sectional quality, relative density, defects, microstructure and mechanical property were investigated and analyzed based on multilayer and mechanical experiments. The surface roughness with CLTS is investigated by comparing the surface quality with low and high layer thicknesses. The study of high-density is aimed at controlling the quality by elucidating the formation mechanism of

defect. The microstructure and mechanical properties were investigated to further understand the performance of the CLTS. The research in this paper will improve the problem of increased efficiency but decreased quality brought about by the use of high layer thicknesses. Due to the unstable nature of the process, there are still many uncertainties in the morphology and microstructural patterns of the produced parts. Experimental studies on a large number of specimens made using different process parameters are often a direct and routine way to understand the effect of these parameters on the characteristics of the specimens produced. The present research may make it possible to use the right layer thickness for the right part.

2 Experimental details

2.1 Materials and experimental equipment

The powder is a subspherical particle as shown in Fig. 1a under scanning electron microscopy with a particle size range of 15–53 μm (Fig. 1b). The particle size distribution was D10: 16.4 μm, D50: 32.13 μm and D90: 57.54 μm. The Ti–6Al–4 V powder is highly spherical and relatively homogeneous, and the chemical composition of the powder is shown in Table 1. The parts were performed on an AM400 (Renishaw plc, London, UK) machine in an enclosed chamber filled with argon as a protective gas, as shown in Fig. 2a. The AM400 adopts a pulsed-mode laser mode Nd:YAG laser with a maximum forming power of 400W. The wavelength is 1075 nm, and the laser beam diameter is 70 μm. The preset scanning strategy is based on the curved scanning strategy, that is, the angle between the Nth layer and the N + 1th layer is 67°, as shown

in Fig. 2b. The physical drawing of the tensile parts fabricated in accordance with Fig. 2d is shown in Fig. 2c. The multilayer structures were sectioned using a wire cutting machine (Cmne, Beijing, China), and the surface morphology and metallography were observed using a KEYENCE (VK-X200, KEYENC, Osaka, Japan) ultra-deep field 3D microscope and (Phenom XL, Phenom-World, Eindhoven, The Netherlands) scanning electron microscope. Metallographic parts were ground and polished according to standard metallographic procedures and then etched with a mixture of 2 mL HF, 6 mL HNO³ and 90 mL H₂O in kroll reagent. The surface roughness of the formed parts was illuminated by a 3D laser scanning microscope (SZ-2000, ASI, UT, USA). Five measurements were averaged to eliminate chance errors. The tensile parts were stretched at room temperature using a universal tensile tester (5966; Instron, Boston, MA, USA) with the stretch rate set to 0.01 mm/s. Three measurements were averaged to eliminate chance errors.

The experiment uses Archimedes’ principle to measure the relative density of the specimens, and the relative density of the specimens is calculated using Eq. 1:

$$\rho_r = \frac{\rho}{\rho_o} * 100\% \tag{1}$$

where ρ_r is the relative density, ρ_o is the theoretical density and ρ is the actual density. The actual density is measured by drainage method and calculated by Eq. 2:

$$\rho = \frac{W_{air} * \rho_{H_2O}}{(W_{air} - W_{H_2O} - W_{line})} \tag{2}$$

where, W_{air} is the gravitational measurement of the specimen in air, W_{H_2O} is the gravitational measurement of the specimen in water, W_{line} is the gravitational measurement of the

Fig. 1 Powder (a) morphology of Ti–6Al–4 V powder; (b) particle size distribution of Ti–6Al–4 V powder

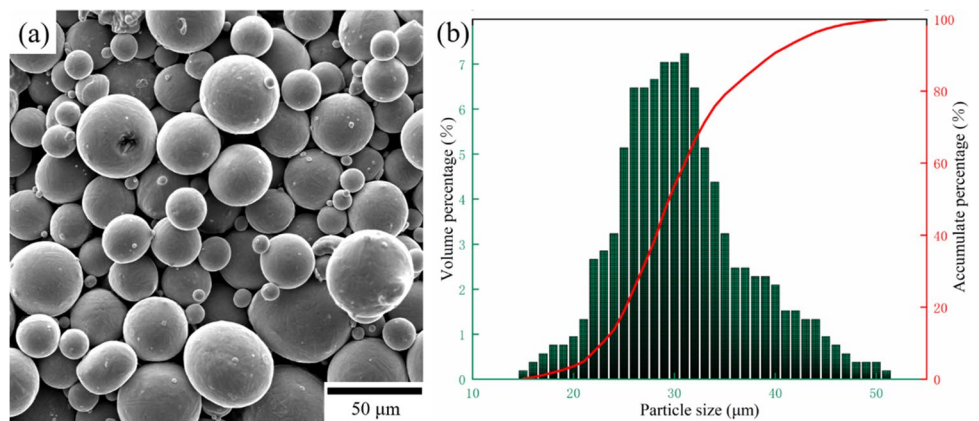
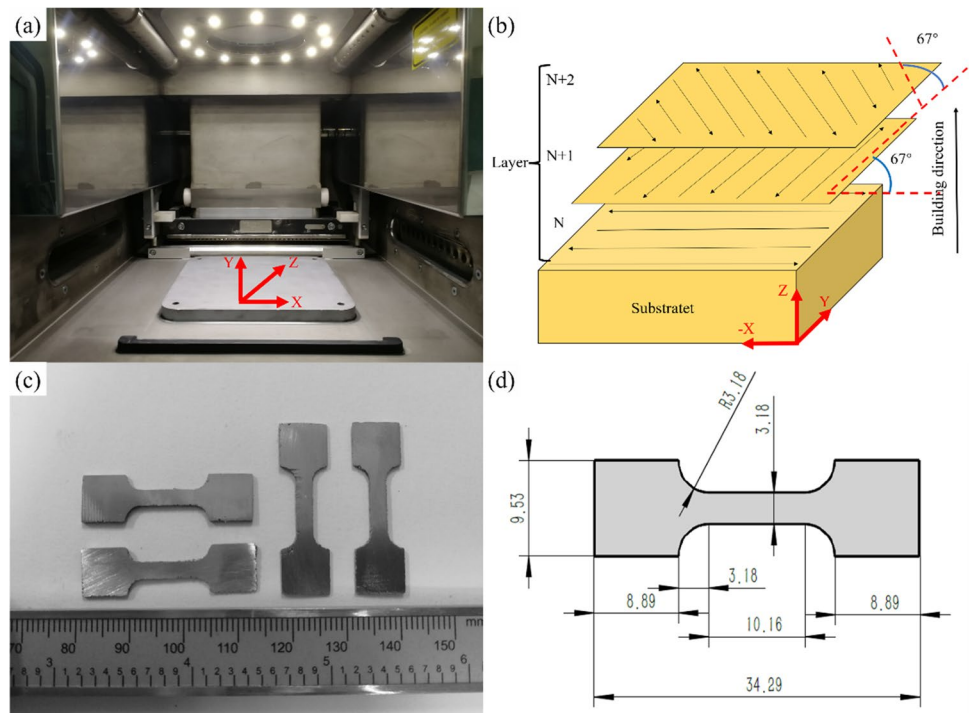


Table 1 Chemical composition of Ti–6Al–4 V powder used in the experiments

Element	Ti	Fe	C	O	N	H	Al	V
Content (wt. %)	Balance	0.028	0.023	0.0634	0.0026	0.002	6.23	4.09

Fig. 2 (a) Experimental equipment; (b) schematic of the meander scan strategy; (c) tensile parts; (d) dimensions of tensile parts



thin line used to hang the specimen and ρ_{H_2O} is the density of water. To avoid chance errors, the densities of each specimen were measured three times and averaged. To improve the statistical quality, the Archimedean drainage method and the cross-sectional method were used to calculate the relative densities of the specimens, and the statistical results were obtained by taking the average values. Micrographs of the specimen sections were analyzed and measured, and the defect area $A_{Defects}$ of each specimen section and the total section area A_{Total} were counted using ImageJ image analysis processing software with the following equation:

$$\rho = \left(1 - \frac{A_{Defects}}{A_{Total}} \right) * 100\% \quad (3)$$

2.2 Experimental methods

The manufacturing strategies of CLTS and IPLT were experimented with the aim of improving fabricating efficiency and ensuring fabricating quality. Within this paper, the result of three sets of experiments were presented, namely, low layer thickness fabrication, high layer thickness fabrication achieved by IPLT and CLTS. The part is divided into 50 μm pieces, and the laser processes the powder using 50 μm process parameters for each layer to achieve the LLTF strategy, as shown in Fig. 3a, d. A group of three 50- μm sliced layers with a total layer thickness of 150 μm is used, and the laser is spaced two layers apart to process the powder with 150- μm process parameters to achieve the IPLT strategy, as shown in Fig. 3b, e. The part is divided into 50- μm pieces

and divided into two groups, the first group of three pieces as a group and the second group of one piece, and the laser is spaced two layers to process the powder with 150- μm process parameters, and then the laser processes one layer of 50 μm powder with 50- μm process parameters, as shown in Fig. 3c, f. IPLT enables efficient manufacturing, and CLTS can improve the manufacturing quality of parts based on IPLT. This paper focuses on verifying the stability and practicality of the manufacturing process of CLTS.

Multilayer parts were prepared according to the parameters shown in Table 2 to evaluate the quality of the process parameters. The laser power, exposure time, point distance and hatch spacing of LLTF were set to 280–380W (in an increment of 100W), 80–160 μs (in an increment of 20–40 μs), 35–80 μm (in an increment of 15 μm) and 50–110 μm (in an increment of 20 μm), respectively. The laser power, exposure time, point distance and hatch spacing of IPLT were set to 280–380W (in an increment of 100W), 100–220 μs (in an increment of 20–40 μs), 25–65 μm (in an increment of 10–15 μm) and 50–110 μm (in an increment of 20 μm), respectively. The experimental parameters for setting the CLTS based on the experimental results of LLTF and IPLT are shown in Table 3. The laser power, exposure time, point distance and hatch spacing for high layer thickness were set to 380 W, 200–240 μs (in an increment of 20 μs), 50 μm and 110–270 μm (in an increment of 40 μm), respectively. The laser power, exposure time, point distance and hatch spacing for thin layer thickness were set to 280W, 100 μs , 35 μm and 70 μm , respectively.

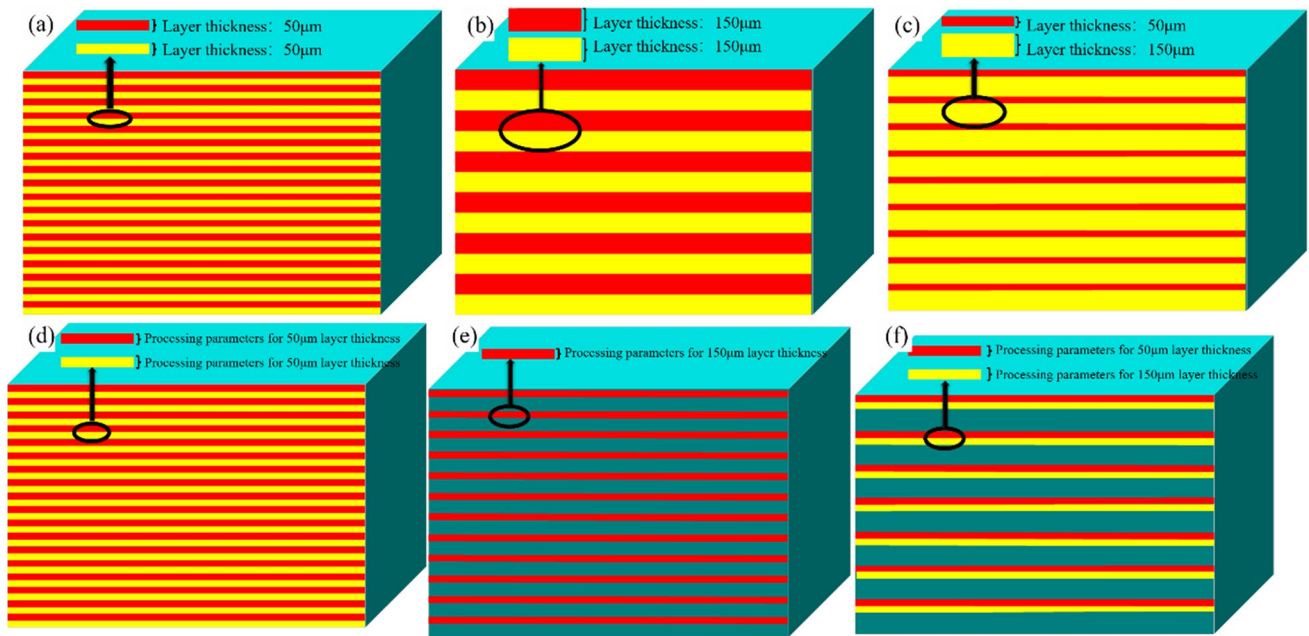


Fig. 3 Layering schematic (a–c) layer thickness distribution; (d–e) distribution of laser process parameters

Table 2 The process parameters of LLTF and IPLT

Parameter	Value	Increment	Value	Increment
Layer thickness (μm)	50 (LLTF)		150 (IPLT)	
Laser power (W)	280–380	100	280–380	100
Exposure time (μs)	80–160	20–40	100–220	20–40
Point distance (μm)	35–80	15	25–65	10–15
Hatch spacing (μm)	50–110	20	50–110	20
Atmosphere	Oxygen target < 200 ppm		Oxygen target < 200 ppm	

Table 3 The process parameters of CLTS

Parameter	Value	Increment	Value	Increment
Layer thickness (μm)	50		150	
Laser power (W)	280	–	380	–
Exposure time (μs)	80	–	140–220	20
Point distance (μm)	35	–	35	–
Hatch spacing (μm)	110	–	110–270	40–50
Atmosphere	Oxygen target < 200 ppm		Oxygen target < 200 ppm	

3 Results and discussion

3.1 Surface quality

Based on the manufacturing principle of AM, the surface characteristics of the parts fabricated by LPBF reflect the manufacturing quality to some extent. Layer thickness plays a key role in the surface quality and surface roughness during LPBF [24, 25]. High surface roughness can impair the performance of the part, which is a typical drawback of LPBF. The surface roughness is not only related to the incidental adhesion of large powder particles, but also to the layer-by-layer stacking of materials and the formation of inhomogeneous regions. The area circled in red in Fig. 4 is the roughness area of the upper surface of the formed specimen measured, and the measurement range is 10 mm × 3 mm. Comparing the roughness of the upper surface of the fabricated specimens as shown in Fig. 4a–d and e–h, it can be found that the LLTF-fabricated surface quality is better than the IPLT-fabricated surface quality. The surface roughness of LLTF is between 15 and 25 μm, while IPLT is higher than 50 μm. The surface roughness of IPLT is higher than that of LLTF, which also leads to a worse surface roughness than the relevant literature with LLTF formed specimens [26, 27].

The surface quality and surface roughness of the CLTS-based parts are shown in Fig. 5. The overall surface quality is better than IPLT and worse than the LLTF, which is in line with expectations. The surface roughness becomes larger as the exposure time increases because the longer

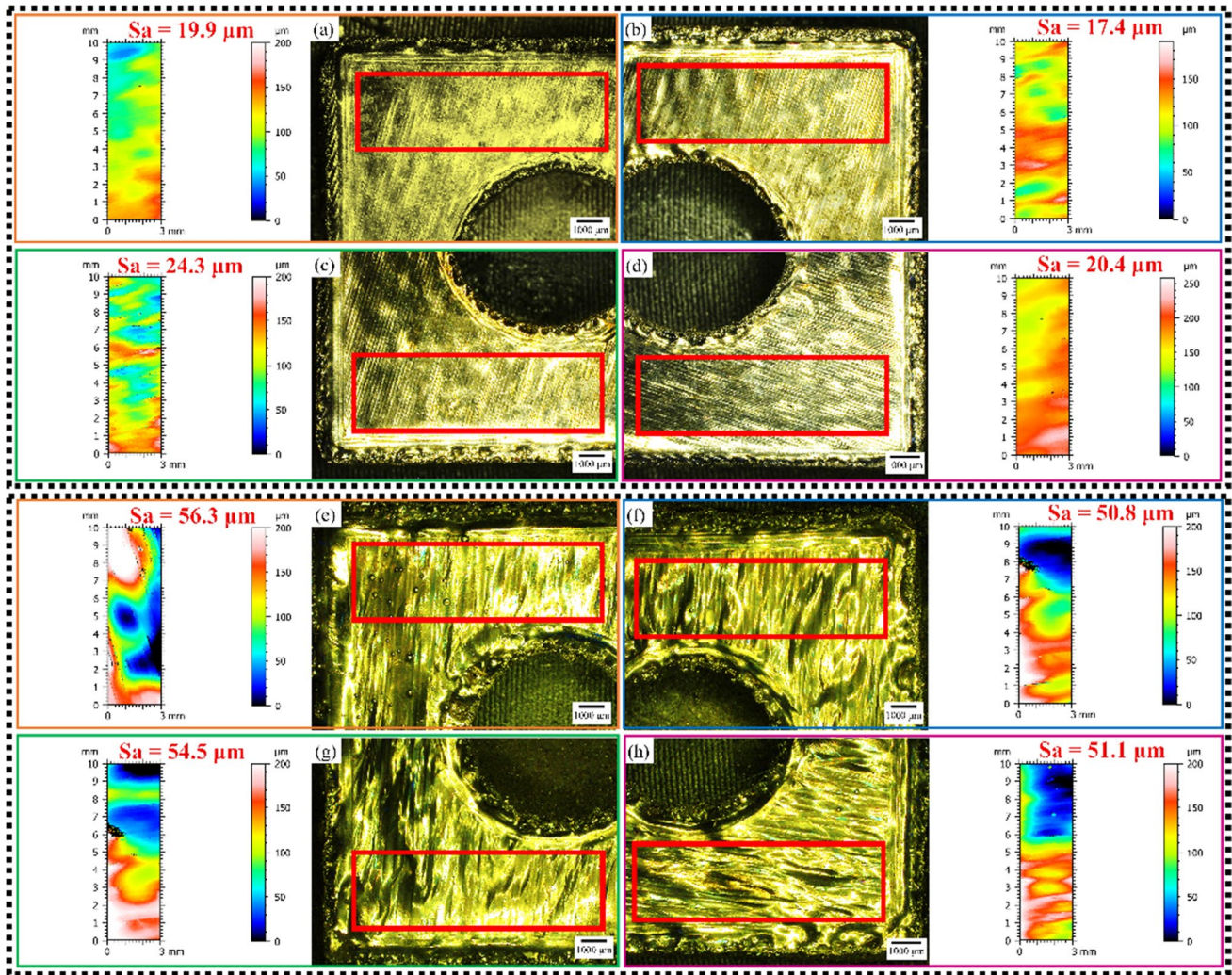


Fig. 4 Surface quality and surface roughness (a–d) LLTF-fabricated parts; (e–h) IPLT-fabricated parts

dwelt time tends to cause process instability and leads to spattering during the forming process, as shown in Fig. 5. Moreover, due to the cumulative effect, the surface continues to deteriorate, and it is difficult to obtain a smooth surface [28]. The hatch spacing has a large impact on the surface quality, which is determined by the energy density. The right energy density can form parts with low surface roughness. As the surface roughness changes the overall surface roughness has a tendency to first decrease and then increase. Smaller hatch spacing can obtain excellent surface quality when the exposure time is short, and larger hatch spacing is more conducive to obtaining lower surface roughness when the exposure time is extended. After optimizing the process parameters, the surface quality of CLTS is similar to that of LLTF, and the minimum surface roughness between 22 and 23 μm can be obtained.

3.2 Relative density

During the LPBF manufacturing process, many parameters must be kept within narrow limits to ensure high product quality and stability. Figure 6 shows the relative densities of the parts based on LLTF and IPLT. It can be observed that the process parameters have a large influence on the cross-sectional quality of the parts. Figure 6a shows the relative density and cross-sectional characteristics of the LLTF at the same hatch spacing of 70 μm . Shorter exposure times are more conducive to high relative density molding for small point distances, and larger point distances require longer exposure times to melt more powder. The relative density profiles for fixed point distance of 35 μm and adjusted hatch spacing are shown in Fig. 6b. Shorter exposure time is more conducive to high quality forming of LLTF, while

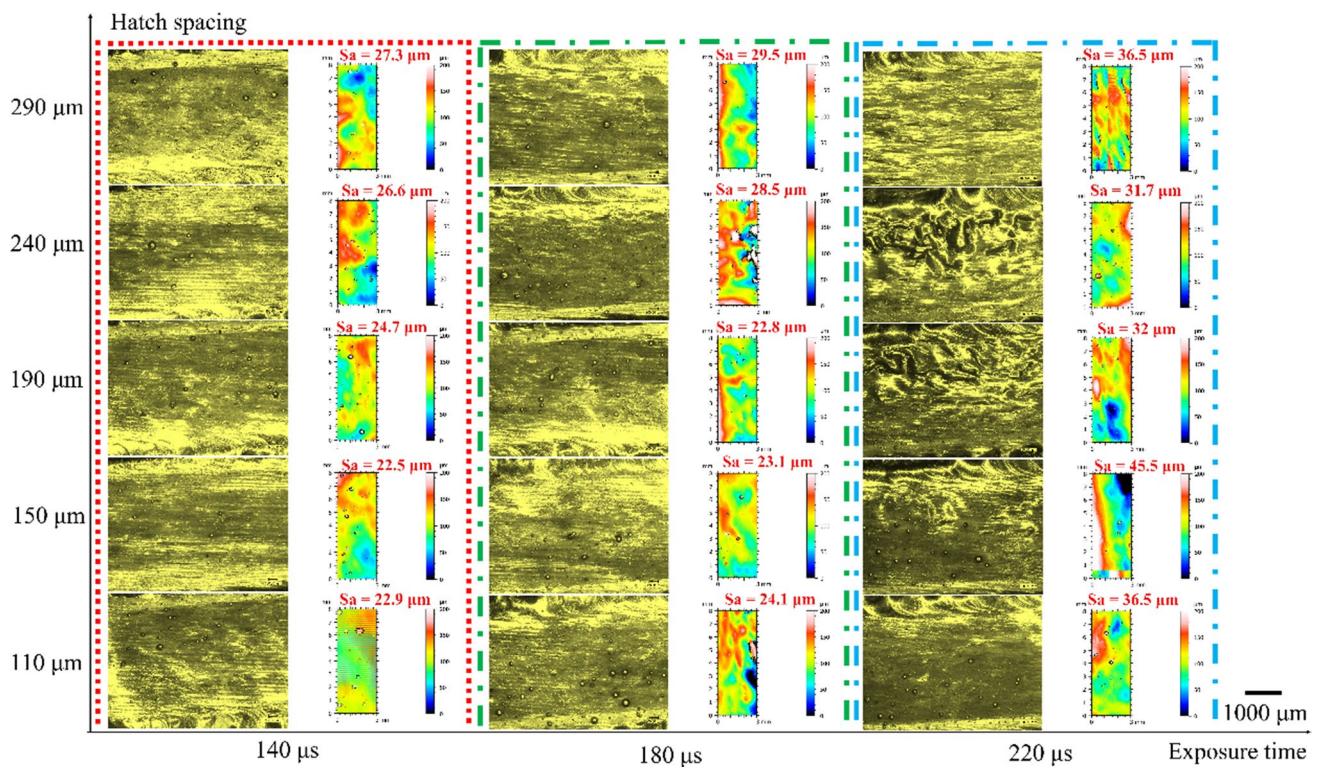


Fig. 5 The surface quality and surface roughness of the CLTS-fabricated parts

the relative density shows a greater tendency to float as the exposure time increases. As shown in Fig. 6a–b, the two laser powers have roughly the same trend at certain parameters, and the two laser powers are sufficient to form the better specimens. Since a small layer thickness is used, the laser power should be chosen to be smaller. This is due to the increase in laser power leads to poorer edge effects [29]. The range of process parameters for LLTF is suitable: exposure time is 80–100 μm and below, the point distance is 50 μm or less and the hatch spacing can be increased appropriately to improve the relative density.

Figure 6c shows the relative density and cross-sectional characteristics of the IPLT at the same hatch spacing of 70 μm . When the hatch spacing is 70 μm , more un-melted defects occur at the point distance of 50–65 μm (i.e. the point distance is higher than 50 μm), which results in lower relative densities (all relative densities are lower than 99%). Better cross-sectional quality can be obtained when the point distance is 25–35 μm . For the same exposure time, the relative density increases as the point distance decreases and the cross-sectional quality increases. This is due to the reduction of the point distance is conducive to a more concentrated energy density at the same location to promote the full melting of the powder. As shown in Fig. 6d, the relative density of hatch spacing is low at 90–110 μm when the point distance is 35 μm . This is due to the decrease in lap rate caused

by increasing the hatch spacing, which tends to lead to the appearance of irregular porosity, which is the same reason for the formation of un-melted defects caused by increasing the point distance at the same hatch spacing. The combination of shorter exposure times and smaller hatch spacing yields better cross-sectional quality with higher relative density. The combination of longer exposure time and larger hatch spacing can achieve higher relative density and better cross-sectional quality. This is due to the LPBF fabricated parts are related to the combination of process parameters and laser energy density, and a better combination of process parameters for IPLT that is suitable is: point distance of 35 μm or less (When the laser power is high 380W, point distance can be extended to 50 μm), exposure time higher than 120 μs , laser power should be used 280–380W higher parameters, hatch spacing should be used higher than the parameters of 70 μm .

Figure 7 shows the cross-sectional characteristics and relative densities of the LPBF fabricated parts. Compared with Fig. 6, the defects in Fig. 7 are only balling effect and a small amount of porosity in the part due to sputtering. This shows that the use of low layer thickness after the adoption of CLTS is beneficial to improve the quality of LPBF fabricated parts. As shown in Fig. 7, the relative density

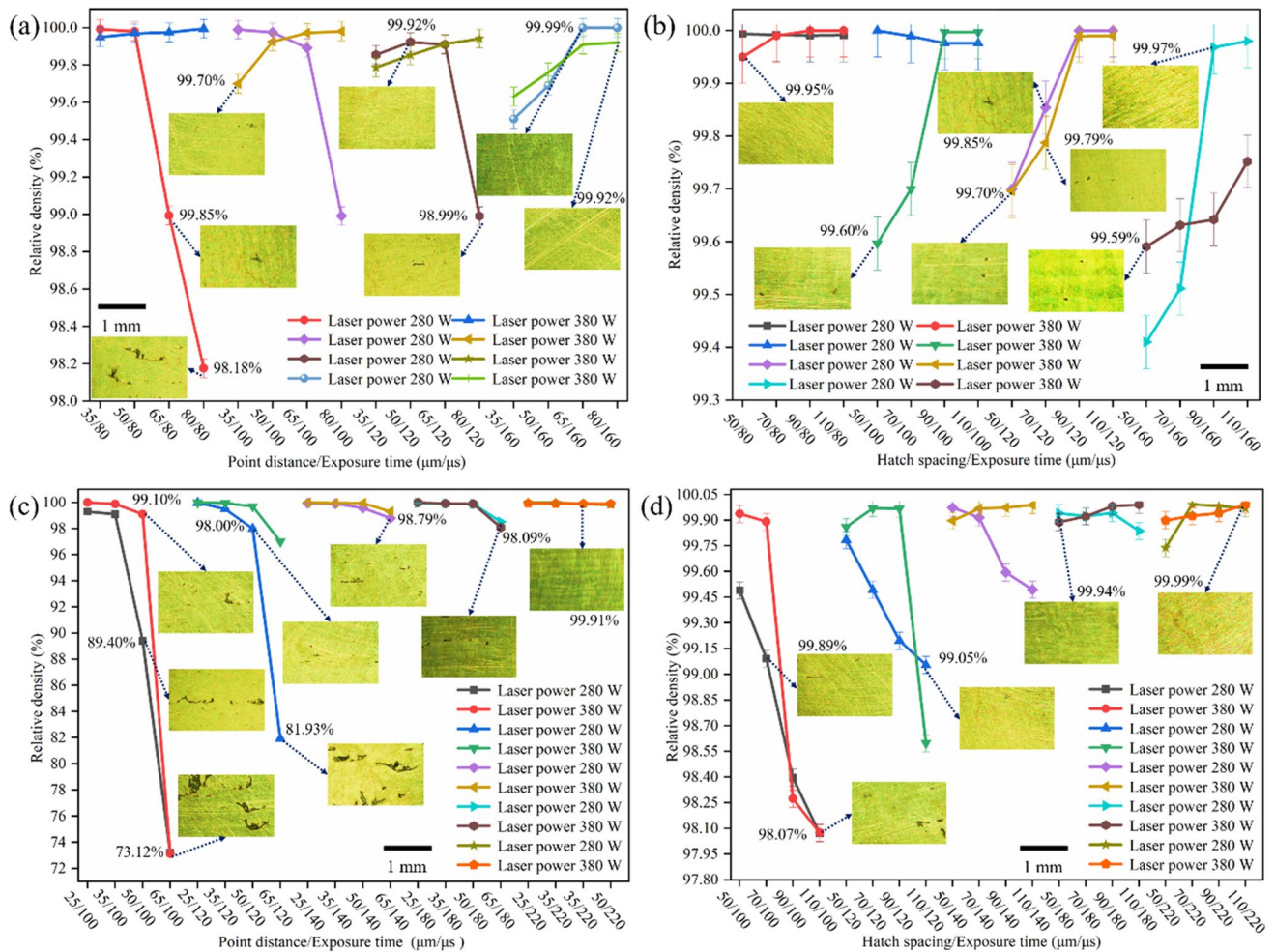


Fig. 6 Cross-sectional characteristics and relative densities of LLTF-fabricated parts with (a) the same hatch spacing, (b) the same point distance; cross-sectional characteristics and relative densities of IPLT-fabricated parts with (c) the same hatch spacing, (d) the same point distance

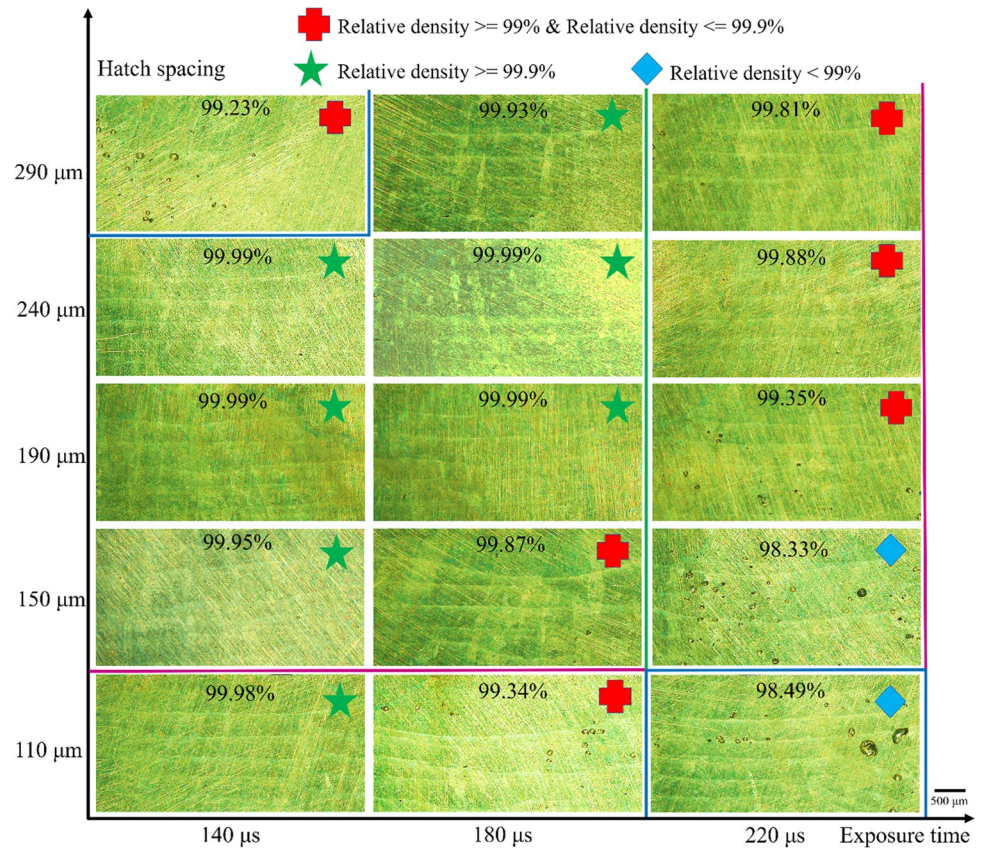
decreases as the exposure time increases. This is due to the extended exposure time, which causes the molten pool to remain liquid for a long time, allowing easy flow and diffusion. In addition, prolonged exposure to a particular exposure point tends to produce more splatter, which results in poorer cross-sectional quality. The black inclusions in Fig. 7 are inclusions inside the specimen caused by sputtering. Therefore, sputtering has a greater effect on the forming density than porosity. Increasing the hatch spacing is beneficial to improve the cross-sectional quality of LPBF fabricated parts when the exposure time is 140–180 μs. This is due to the fact that increasing the hatch spacing can disperse the laser energy density to rationalize the energy density.

3.3 Defect formation

Internal defects are an important factor in the failure of a part and in the quality of its manufacture. Therefore, analyzing the causes of defect formation and then adjusting the

process parameters and manufacturing strategy is an important way to ensure the quality of the specimen. Un-melted defects between the molten pools, spherical defects and microporous defects were formed inside the specimens fabricated by LLTF and IPLT strategies. Spherical defects and microporous defects were formed inside the CLTS specimens. Since IPLT is manufactured with high layer thickness, there are more un-melted defects inside the specimen than LLTF, as shown in Fig. 6a, c. In addition, un-melted defects between the molten pools can disappear completely with the adjustment of the process parameters. Spherical defects can be found in all three strategies, IPLT has the largest size of spherical defects with the size range of 153–180 μm. The smaller size but higher probability of occurrence of spherical defects in CLTS may be due to the appearance of spherical defects is exacerbated by lower thickness forming after higher thickness forming, but remelting can mitigate the effect of some defects. Microporous defects are also present in all three strategies, and the size and probability of

Fig. 7 Cross-sectional characteristics and relative densities of the CLTS fabricated parts



occurrence are similar, ranging from 5 to 25 μm . Figure 8a, d shows the un-melted defects, which is caused by insufficient energy input during the manufacturing process. A lower laser energy input results in a smaller molten pool width, which leads to insufficient overlap between melt tracks. Poor interlayer bonding may also result in un-melted defects if the laser energy input is too low and the molten pool does not have sufficient penetration depth. As shown in Fig. 9a, the metal powder was not completely melted due to the improper selection of process parameters and insufficient overlap of the same or adjacent layers [30, 31]. Un-melted defects will result in the part containing a large amount of un-melted metal powder inside, as shown in Fig. 8a, d.

The LPBF process undergoes complex thermal changes, and the liquid metal solidifies with shrinkage pores due to the different filling states of the melt and different cooling rates. As shown in Fig. 8c, f, h, the shrinkage holes are irregular in shape and larger than the air holes. Due to the fast solidification rate, the liquid metal does not have enough time to diffuse completely, which may form significant shrinkage holes. Even if the content of shrinkage holes is small, it may impair the mechanical properties of the alloy [32]. As shown in Fig. 8c, f, i, the formation of pores in the manufacturing process is caused by gas mixing into the molten pool. Gases between the powder particles may be dissolved in the molten pool, and due to the high cooling

rate during solidification, the dissolved gases cannot come out of the molten pool surface until solidification occurs. As shown in Fig. 9b, the porosities are formed and retained in the fabricated part. Porosities can also be formed due to the mixing of hollow powder during the manufacturing process (Fig. 9c). In addition, the molten pool temperature is usually high during the forming process and the gas is highly soluble in the liquid metal, making it easier to enrich [33]. Porosities are very common and unavoidable, but their content is low and has little effect on the mechanical properties of the alloy. However, when a cyclic load is applied, the porosities become stress concentration zones and reduce the cyclic strength [34].

Figure 8b, e, g shows the internal spheroidal defects due to spattering. The spattering is mainly attributed to the thermodynamic, kinetic and metallurgical instability of the small molten pool [35]. Spattering is a manifestation of instability that occurs when the interaction between the laser, the powder, the ambient atmosphere and the solidified part generates physical and chemical reactions, as well as the metallurgical properties of the molten pool in terms of rapid melting and solidification. The laser beam irradiates the powder surface and the spatter particles produced under the influence of recoil pressure; Marangoni effect and melt pool thermal effect solidify during the spatter process [36]. Due to the different spattering distances, the

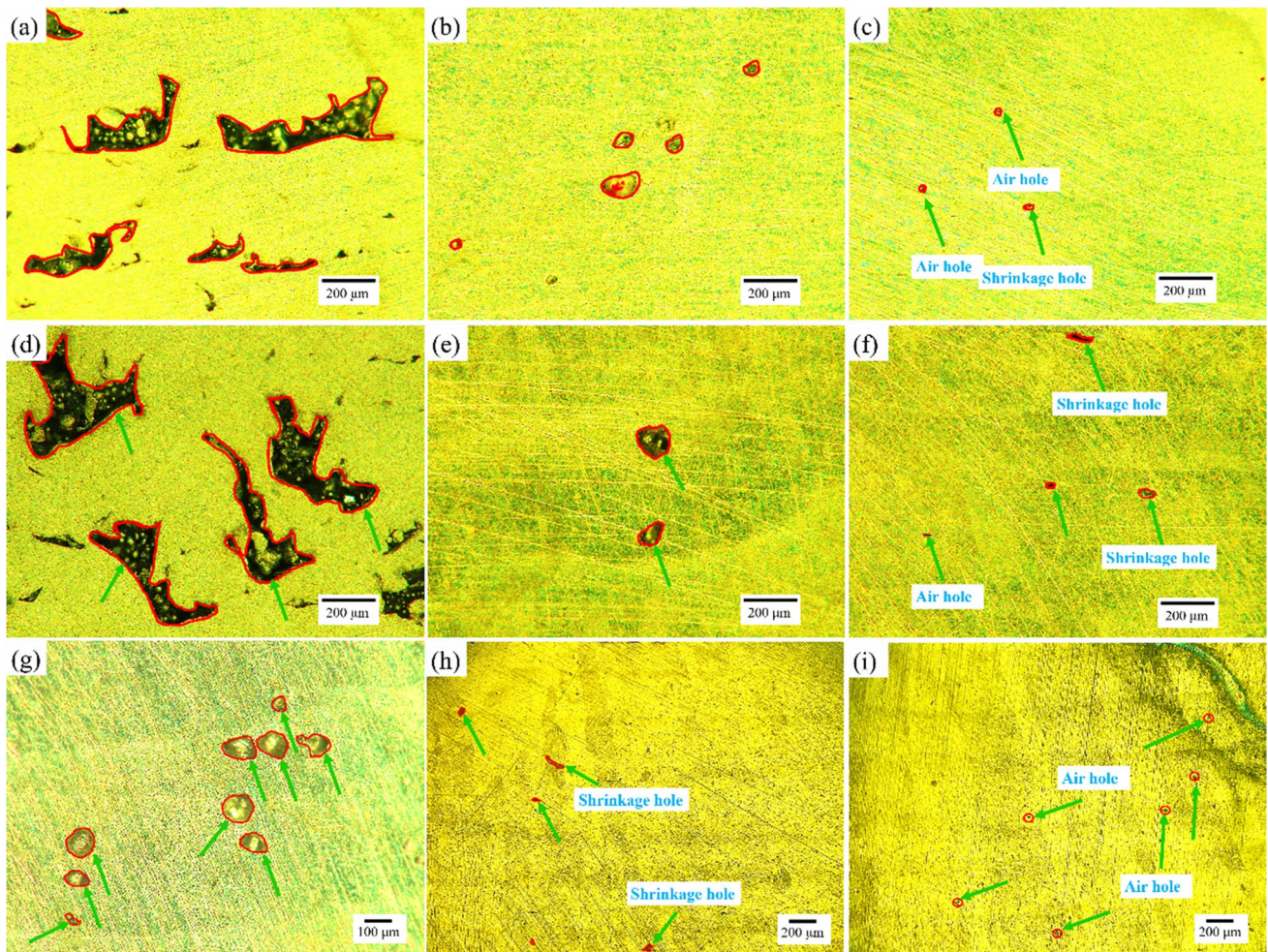


Fig. 8 Manufacturing defects (a–c) LLTF internal defects; (d–f) IPLT internal defects; (g–i) CLTS internal defects

droplets contract freely and form spherical particles of different shapes. The LPBF manufacturing process cannot guarantee the absence of oxygen content in the building chamber, even if argon is used as a protective gas. After the molten powder leaves the molten pool during the manufacturing process, the splattered particles will react with oxygen to produce oxides. This leads to an increase in the oxygen content of the splash particles. The fumes generated when metal materials are melted by laser lead to increased levels of carbon-based atmospheres in building rooms. As the splattered particles leave the melt pool and solidify again, the carbon-based atmosphere in the building chamber penetrates into the metal liquid, which can lead to an increase in the carbon content of the spatter [36]. As shown in Fig. 9d, some spatter particles fall into the molten pool to form internal balling effect. Some spatter particles on the surface of the solidified part to form a spherical surface (as shown in Fig. 9e). Some particles fall into the un-melted metal powder (as shown in Fig. 9f), and the spatter particles mix with the manufacturing powder,

thus affecting the stability of the LPBF process and the mechanical properties of the manufactured part. Because the spatter particles hinder the powder laying and laser radiation, there are holes and un-melted powder particles in the melting zone [36]. Impurities in LPBF manufactured components seriously affect the mechanical properties of metal parts and pose a threat to the stable operation of the recoater blade [37]. According to the spattering formation mechanism, spattering is inevitable. Through related process control, the generation of spattering can be reduced, as shown in Fig. 7.

The un-melted defects (Fig. 8a, d) can be completely eliminated by adjusting the process parameters, and the un-melted defects are eliminated when the IPLT screened process parameters are applied to CLTS. Since the energy density of CLTS changes during the manufacturing process, the high energy density used for low layer thicknesses allows partial melting of parts fabricated in high layer thicknesses, thus optimizing the manufactured parts and obtaining high relative density parts. As shown in Fig. 8g–i, the CLTS

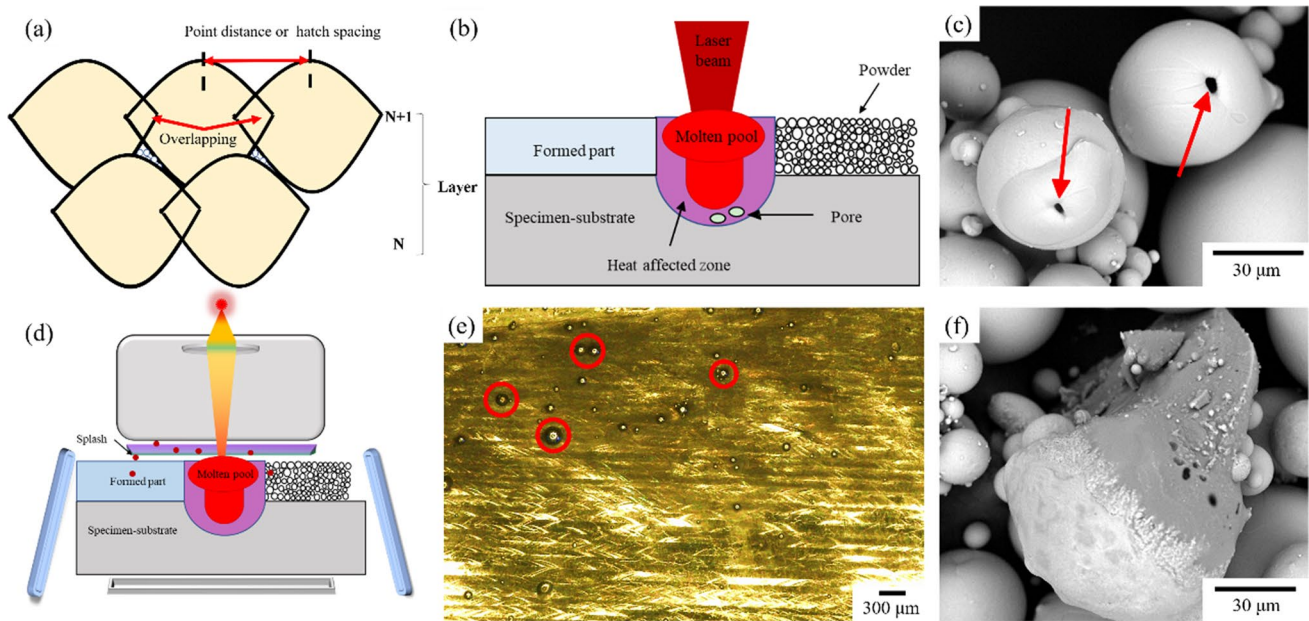


Fig. 9 Schematic diagram of defect formation (a) un-melted defect; (b) porosity; (c) hollow powder; (d) spattering; (e) surface balling effect; (f) spatter particles

fabricated parts contain only balling effect and porosity inside, which shows the excellent manufacturing quality.

3.4 Microstructure

The microstructure of Ti–6Al–4 V is usually a β -phase above 980 °C [38] and a mixture of α and β below this temperature. As shown in Fig. 10a–e, the microstructure contains mainly long columnar β grains that grow toward the fabrication direction due to the significant thermal gradient in the LPBF process. The energy density of the laser source obeys the Gaussian distribution, with the center temperature higher than the sides. Therefore, the β -phase is easily formed in the central region of the laser, while the mixed phases of α and β are easily formed in the heat-affected regions on both sides of the laser. The transformation of β -phase to α -phase depends mainly on the cooling rate [39]. Ti–6Al–4 V transforms to acicular martensite (α') at high cooling rates (above 410 °C/s) [21]. As shown in Fig. 10, the CLTS fabricated parts have the acicular martensite α' occupying and filling the columnar β grains. The energy density is higher for both high and low layer thicknesses during CLTS, thus generating a larger temperature gradient, which favors the formation of acicular martensite (α'). As shown in Fig. 10f–j, acicular martensite (α') is generated and arranged into a mesh basket organization structure with different dimensions and orientations.

Compared to conventional thermomechanical processing techniques, SLM is characterized by: (a) high temperature gradients (10^6 K/m) and fast solidification and cooling

rates; and (b) a complex thermal history, including directional laser melting and solidification of metal powders, and multiple reheating and cooling cycles of solidified parts. The cooling rate is higher due to the increased thermal conductivity of the specimen compared to the powder bed. On cooling below the β -transformation temperature, a solid-state phase transition will occur. Diffusion-free phase transformation from pristine Ti grains with body-centered cubic structure to hexagonal dense packed α' crystals occurs at high cooling rates. Thus, the α' grains nucleate at the primordial β grain boundaries and grow within their parent β crystals, and the crystal orientation between α' and primordial β follows the Burger relationship [40]. Due to the steep temperature gradient encountered during the build process, the LPBF specimens exhibit a distinct directional solidification microstructure, in which the a columnar β grains grown epitaxially along the build direction can be clearly seen, as shown in Fig. 10. Compared to LLTF and IPLT, CLTS has different heat accumulation effects during the construction process and therefore may affect the thermal gradient as well as the solidification behavior. All three process specimens exhibit a typical directional solidification microstructure, which indicates that the effect of thermal conditions on the forming process using different process strategies is not sufficient to change the solidification pattern. All three processes showed a complete β -phase and an acicular α' martensitic phase, as the cooling rate was higher than 410 °C/s. The solidification cooling rate usually varies with the scanning speed, based on the following equation [41]:

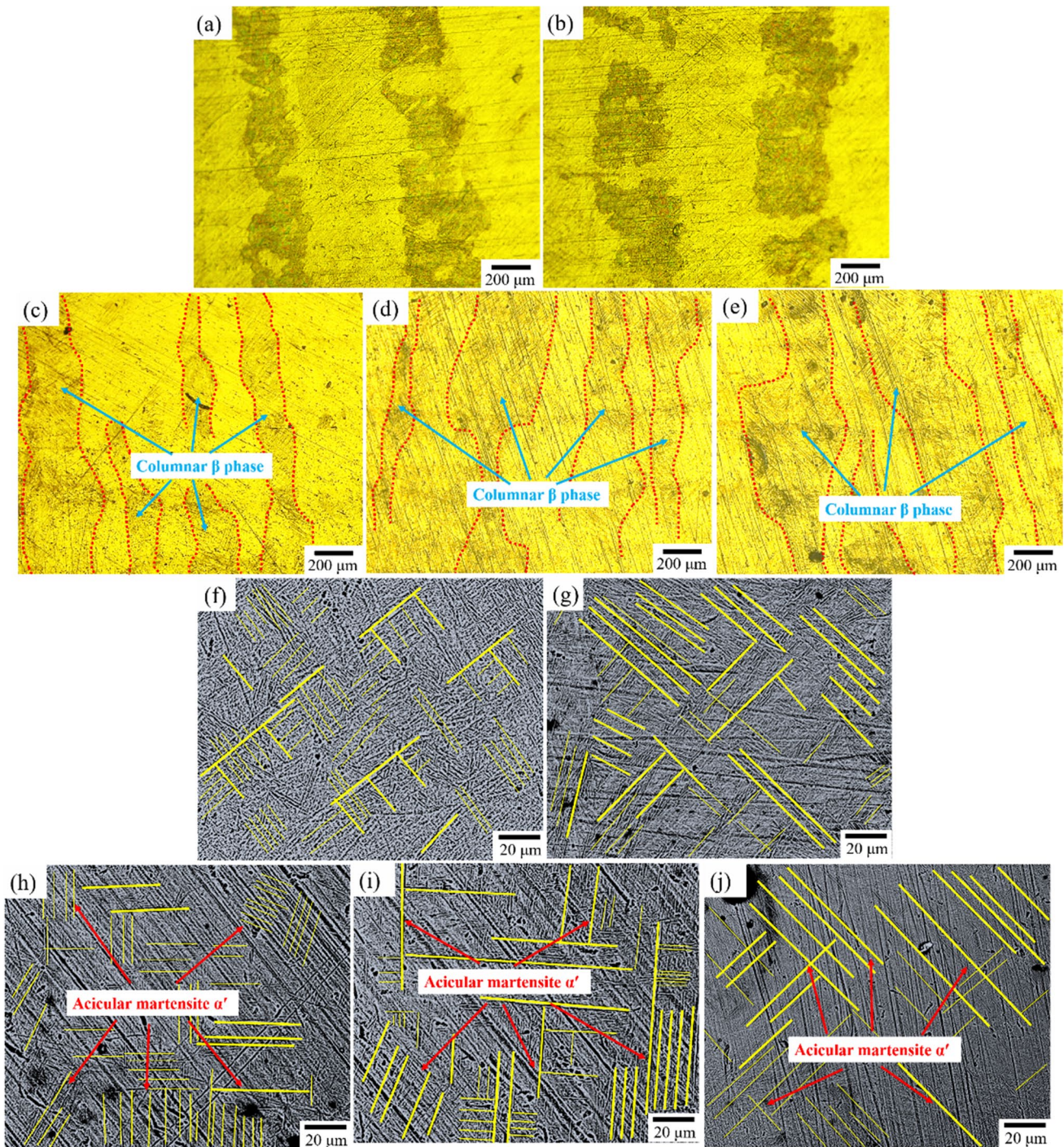


Fig. 10 Microstructure (a, f) LLTF; (b, g) IPLT; (c, h) CLTS-140 μs ; (d, i) CLTS-180 μs ; (e, j) CLTS-220 μs

$$T = (2.07 \times 10^4) V^{1.2} \quad (4)$$

The scanning speed is related to the exposure time, and as the exposure time is extended, the scanning speed is reduced and the cooling speed is reduced. IPLT has higher laser power and longer exposure time than LLTF, so the melt pool temperature is higher. Based on the classical theory of uniform

nucleation and isotropic linear growth during rapid solidification, the relationship between the solidification cooling rate and the β grain size (L , μm) of Ti alloys was derived [42]:

$$L = A \cdot T^{-n} \quad (5)$$

where $A = 3.1 \times 10^6 \mu\text{m} (\text{K/s})^{0.93}$ and $n = 0.93$ for Ti-6Al-4V alloy [43]. The lower the solidification cooling rate, the

larger the β grain size. As shown in Fig. 10a–e, the microstructure of the high-power alloy has wider preferential β grains [44], and IPLT has longer and thicker needle-like bodies than LLTF. As a result, the IPLT has coarsened β grains and longer martensite dimensions. The β grains of CLTS are also coarser than LLTF due to the higher laser power experienced by the CLTS process. The width of columnar β grains is roughly in the range of a few tens to a few hundred micrometers. In contrast, the epitaxial growth distance of the β grains can easily reach 1–2 mm or even span the entire specimen in length [45]. Due to the high cooling rate involved in the LPBF process, all specimens have an acicular martensitic microstructure in the β matrix. Most α' martensite nucleates at β grain boundaries and grows within its parent β grain, although a few α' martensite diffuses into adjacent β grains. Most α' martensitic needles are oriented in an arbitrary direction with respect to the building direction, within the β grains, elongated and strongly textured along the building direction. Their widths fluctuate over a wide range, from a few tens of nanometers to 1–2 μm , while their lengths remain between a few micrometers and tens of micrometers. A large number of crystal defects, such as twins and dislocations, can be observed within the martensitic pin, and these high relative density crystal defects should facilitate the increase in strength and hardness [46]. Flower [47] investigated the effect of grain structure on the ductility of hot worked titanium. In his study, it was concluded that ductility was enhanced with decreasing characteristic sizes. One possible reason for the variation in β -grain width, thickness and length for the three strategies could be due to higher melt pool temperatures, resulting in increased remelting of the lower layers. These higher temperatures may also cause some local annealing. This in turn would promote the epitaxial growth of the first β grains and increase the grain coarsening rate and refine the martensitic phase [48].

By a finer observation, martensite α' can be continuously derived, and the newborn derivative tissue grains are finer than those of the previous generation derivatives. The primary and secondary α' martensites in micron-sized level seem to nucleate and grow during the early stage of heat history and then grow further during the subsequent thermal cycles. Contrarily, the tertiary and quartic α' martensites are believed to be formed during the later stage of heat history, and thus the growth process is inhibited by the boundaries of previously precipitated α' martensites as well as the absence of subsequent thermal cycles [43]. As shown in Fig. 10f–g, the martensitic α' phase of LLTF is finer than that of IPLT, and the martensitic α' phase of CLTS is in the intermediate state, which is determined by the layer thickness and heat input. As shown in Fig. 10h–j, the martensitic α' phases and its derivatives decrease with increasing exposure time. This is attributed to the cumulative effect of thermal cycling in the LPBF process due to the extended exposure time, which

keeps the melt tracks in liquid state for a long time. As the exposure time increases, the melt pool temperature rises, and the cooling rate decreases to form coarser α' grains. The analysis shows that the exposure time has a significant impact on the microstructure of the part, with higher powder layers requiring longer exposure times for adequate melting and therefore larger deviations in the microstructure.

3.5 Mechanical properties

Figure 11 summarizes the results of the mechanical properties of the parts manufactured using different process strategies. It can be seen that tensile strength and yield strengths of all three strategies are higher than those of forging and casting. LLTF has the highest tensile strength and yield strength, and CLTS has better tensile properties than IPLT. The ultimate tensile strength, yield strength and elongation of CLTS were 1107 MPa, 1205 MPa and 6.8%, respectively. The tensile properties of CLTS are similar to those of LLTF, which indicates that a level similar to that of low layer thickness can be achieved using the CLTS. Compared to forging and casting, CLTS produces parts with higher ultimate tensile and yield strengths, but lower elongation. This is due to the presence of the martensitic α' phase which ensures the strength of the part, but reduces the plastic properties.

Figure 12 shows the schematic diagram of the mechanical properties of the specimens constructed in different orientations. The horizontally constructed Ti–6Al–4 V specimens yielded higher strength, while the vertically constructed samples obtained better elongation, indicating the presence of mechanical anisotropy in LPBFed Ti–6Al–4 V specimens [49]. The effective grain size of horizontally placed parts is smaller than the effective grain size of vertically placed parts because the grain boundaries of parts with different placement directions are different, and there are more grain boundaries for horizontally placed parts than for vertically placed ones [50]. Therefore, the strength of horizontally placed specimens is higher than the strength of vertically placed specimens [51]. In addition, cracks preferentially extend along near vertical columnar grain boundaries, and cracks propagate faster in horizontal specimens than in vertical specimens, resulting in lower elongation [52].

Figure 13 shows the average microhardness values of the specimens for different manufacturing strategies at different process parameters. Low layer thickness forming does not require a long exposure time to fully melt the powder and obtain excellent properties to achieve the LLTF strategy. Related studies can be found in our previous published papers [53]. High layer thickness forming requires long exposure times to ensure adequate melting of the powder to achieve the IPLT strategy. According to our previous study, the appropriate interval of exposure time for the IPLT strategy is 140–220 μs . The forming of the high layer

Fig. 11 The mechanical properties of the parts manufactured using different process strategies

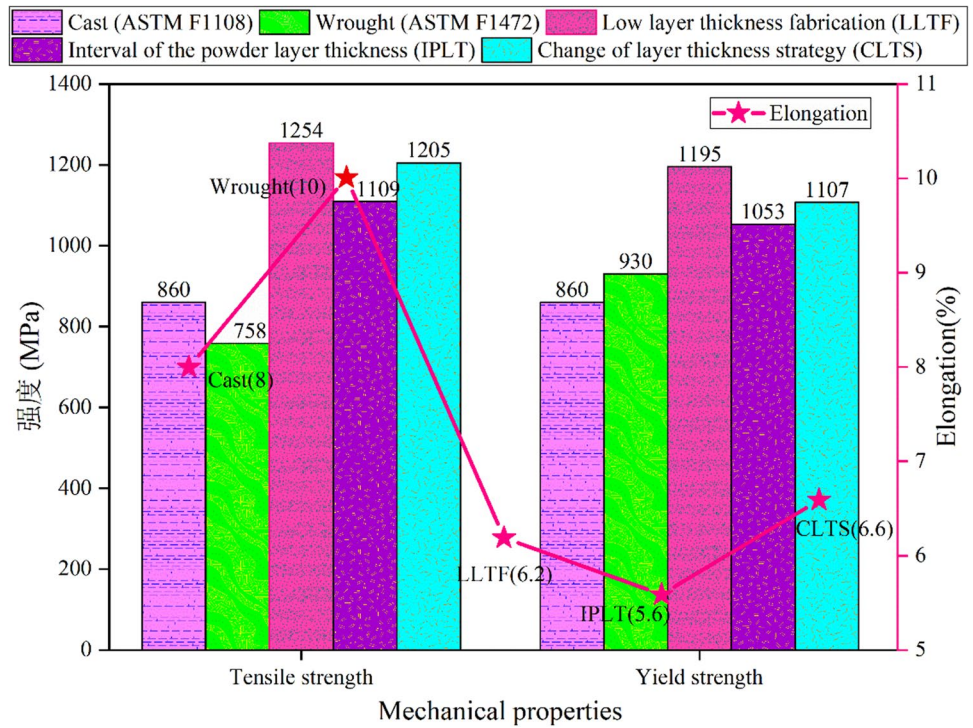
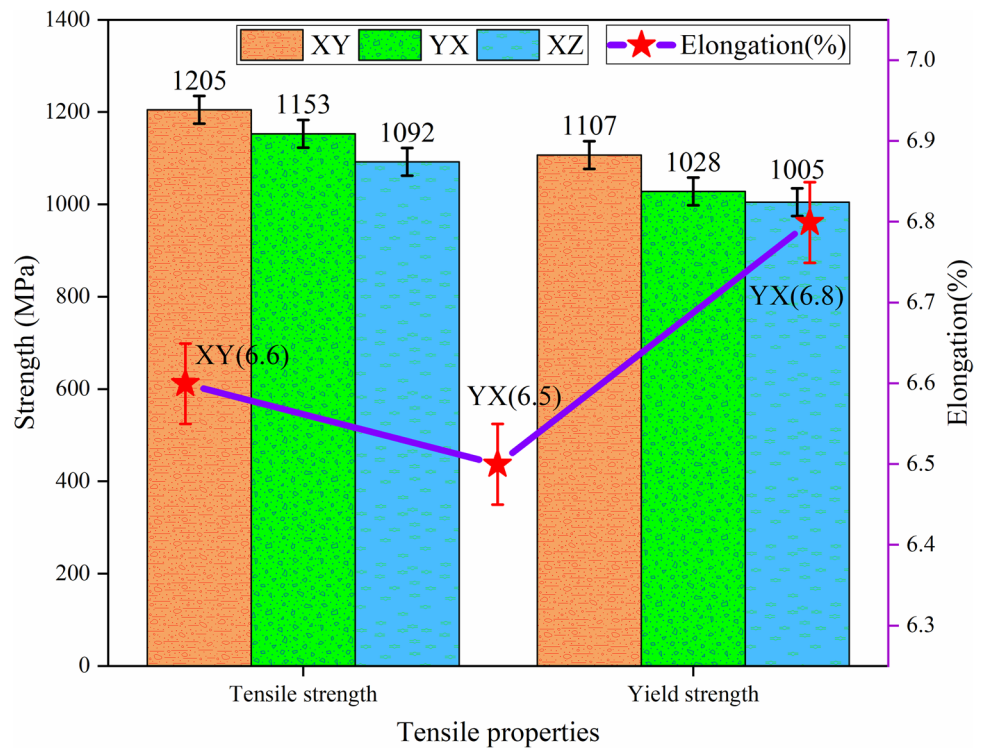


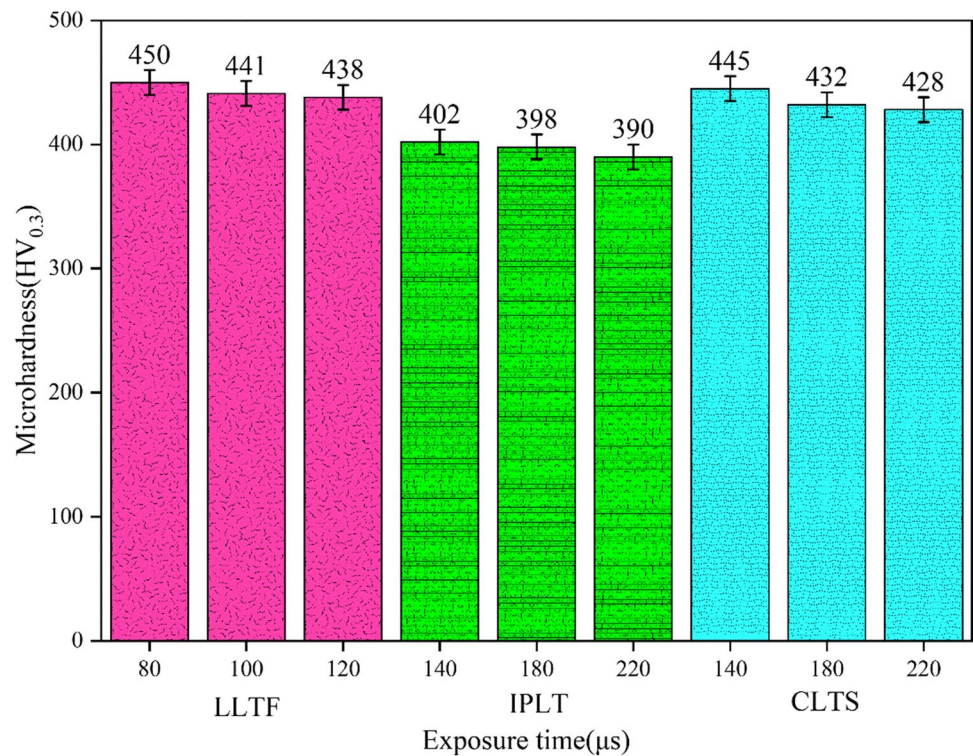
Fig. 12 Mechanical anisotropy of CLTS



thickness of CLTS also requires a high exposure time to ensure adequate melting of the powder. Microhardness is affected by porosity and grain size. As shown in the Fig. 13, LLTF microhardness values can reach up to 450 HV_{0.3}, and IPLT microhardness values can reach as low as 390 HV_{0.3}.

The hardness value of CLTS can reach up to 445 HV_{0.3}, which is similar to the hardness value of LLTF, indicating that CLTS can be comparable to the forming quality of low layer thickness. The microhardness values of all three strategies showed a decreasing trend with increasing exposure

Fig. 13 Microhardness



time, which is due to the fact that prolonging the exposure time decreases the cooling rate and thus leads to an increase in grain size, which is not conducive to further improvement of microhardness.

Figure 14 shows a representative fractogram of the tensile fracture of the Ti–6Al–4 V parts fabricated by LPBF. The morphological characteristics of the tensile fractures of LLTF, IPLT and CLTS are similar, and all have the same defect morphology and fracture morphology [53]. The fracture characteristics of CLTS components are a mixture of ductile fracture, brittle fracture and quasi-dissociative fracture. Oval object resembling the shape of the molten pools can be observed on brittle fracture surfaces (e.g. Figure 14e, f), and small dimples with dimensions of 1–5 μm can be observed on ductile fracture surfaces (e.g., Fig. 14g, h). Low height separation ridges were evident on the quasi-cleaved facet surfaces, which indicated that the LPBF sample fracture had occurred by the formation and the coalescence of micropores, as shown in Fig. 14i. Firstly, in different parts, many destructive crack nuclei are produced at the same time, and then they are expanded into destructive small facets according to the destructive mode, and finally they are torn in a plastic way and connected with the adjacent destructive small facets to form tearing ribs. Inside the fracture there are obvious holes and slag entrapment and lead to a reduction in the overall mechanical properties of the part. Figure 14 clearly shows the defect morphology of porosity (as in Fig. 14a, b), balling effect due to spattering (Fig. 14d) and

slag entrapment (Fig. 14c, d). These defects are the cause of low relative density and poor mechanical properties.

3.6 Productivity calculation

We use the forming efficiency of conventional low layer thickness as a benchmark to compare and study the forming efficiency of specimens. Since the forming efficiency of IPLT is equivalent to that of high layer thickness (150 μm), the forming efficiency of IPLT and LLTF is calculated by Eq. 6. The forming efficiency of CLTS can be calculated as the sum of 75% of IPLT (150 μm) and 25% of LLTF, as shown in Eq. 7.

$$V = \frac{d \times \delta \times h}{t} \tag{6}$$

$$V_{CLTS} = V_{IPLT} * 75\% + V_{LLTF} * 25\% \tag{7}$$

V is the forming efficiency (mm³/s), d is the point distance (mm), δ is the layer thickness (mm), h is the hatch spacing (mm), t is the exposure time (s). Table 4 summarizes the Ti–6Al–4 V forming efficiency. The forming efficiency of LLTF is 2.41 mm³/s, while the forming efficiency of IPLT can reach 9 mm³/s. The forming quality of CLTS using a combination of both processes is similar to that of LLTF, while the forming efficiency is much higher than that of LLTF and higher than that the layer thickness

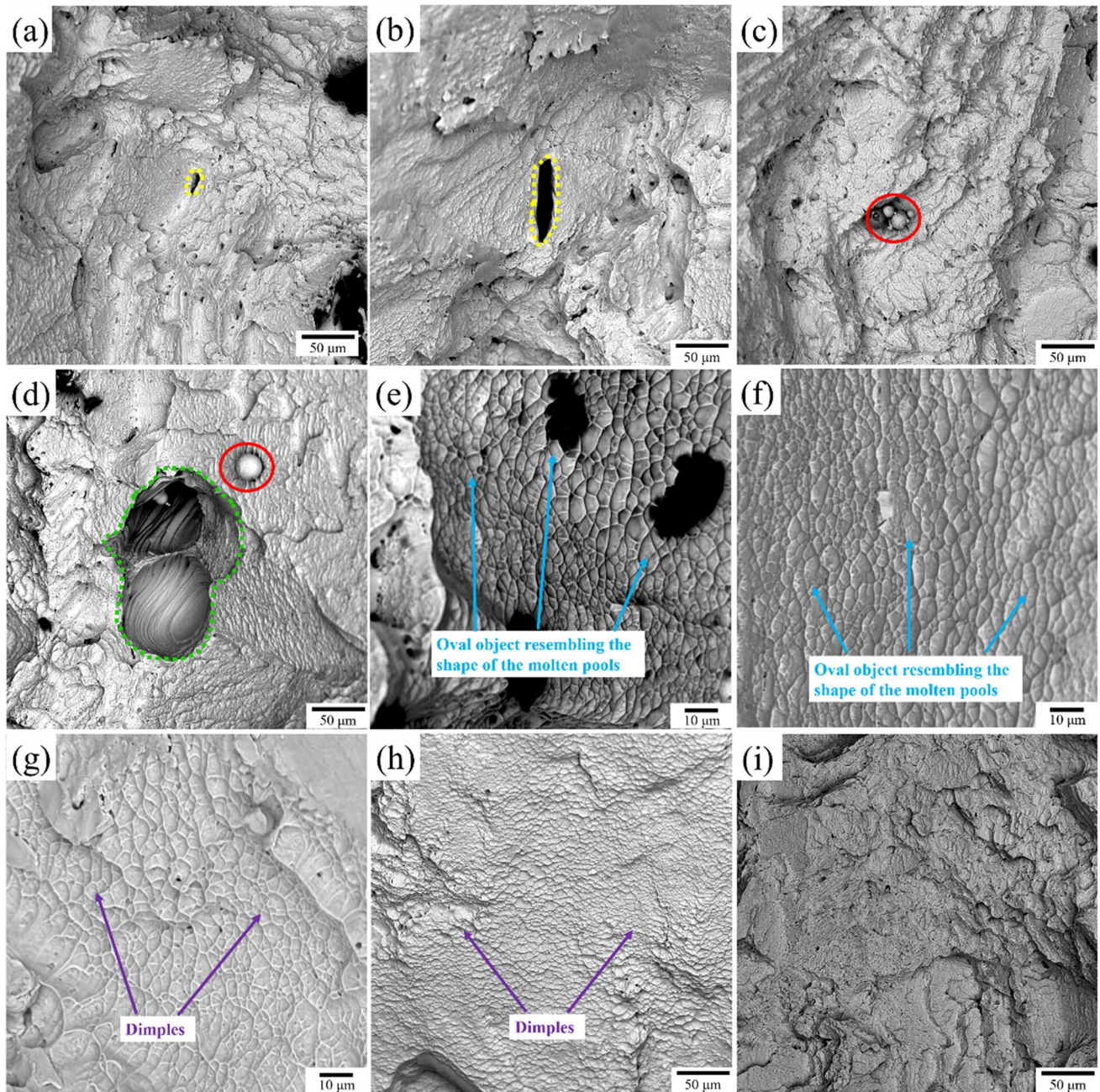


Fig. 14 Fracture morphology of CLTS (a–d) fracture internal defects; (e–i) fracture morphology

Table 4 Ti–6Al–4 V forming efficiency

Layer thickness (μm)	Scanning speed (mm/s)	Hatch spacing (mm)	Point distance (mm)	Exposure time (ms)	Building rate (mm ³ /s)	Reference
50	227	0.1	–	–	1.135	[54]
LLTF	437.5	0.11	0.035	0.08	2.41	In this research
CLTS	437.5/250	0.11/0.24	0.035/0.035	0.08/0.14	7.35	In this research
IPLT	250	0.24	0.035	0.14	9	In this research
200	60	0.6	–	–	7.2	[55]

of 200 μm [54]. The CLTS has better surface quality, relative density and mechanical properties than the parts fabricated by IPLT. Therefore, this paper proposes an efficient fabricating method that can guarantee the manufacturing quality, which can guarantee the quality based on improving the manufacturing efficiency.

4 Conclusion

This experiment verifies the process stability and the optimal fabricating process for the preparation of Ti–6Al–4 V under LPBF conditions by CLTS with alternating 150- μm layer thickness and 50- μm layer thickness. The effects of process parameters on the surface morphology, relative density, defects, microstructure and tensile properties of parts were analyzed by multilayer preparation experiments and tensile mechanics experiments. Our conclusions are as follows.

1. The overall surface quality of CLTS is better than IPLT, which is worse than that of LLTF. The minimum surface roughness of the specimens manufactured by CLTS is similar to that of LLTF in the range of 22–23 μm .
2. When the exposure time is 140–180 μs , increasing the hatch spacing can disperse the laser energy density to rationalize the energy density, which is conducive to improving the cross-sectional quality of CLTS parts. The relative density of most of the fabricated parts is higher than 99%, with the highest densities up to 99.99%.
3. Three types of defects were found in the specimens fabricated with IPLT and LLTF, namely, un-melted defects between molten pools due to improper selection of process parameters, slag defects caused by spattering and porosity defects. Two kinds of defects, slag inclusion defects caused by spattering and porosity defects, were found in the specimens fabricated with CLTS.
4. The martensite of IPLT is longer and thicker than that of LLTF, and the β -grain of CLTS is also coarser than that of LLTF due to the higher laser power experienced. The tensile properties of CLTS were similar to those of LLTF, with the ultimate tensile strength, yield strength, and elongation of 1107 MPa, 1205 MPa and 6.8%, respectively. Due to the anisotropy in the SLM process, the horizontally constructed Ti–6Al–4 V specimens produced higher strengths, while the vertically constructed specimens obtained better elongation.
5. The surface quality, relative density and mechanical properties of CLTS are similar to LLTF, while the forming efficiency is much higher than LLTF, which can reach 7.35mm³/s.

Author contribution All authors contributed to the study conception and design. **PW:** conceptualization, methodology, resources, funding acquisition, writing—review and editing. **DC:** investigation, validation, visualization, writing—original draft. **JF:** methodology, software, visualization, writing—review and editing. **GL:** formal analysis, investigation, data curation. All authors read and approved the final manuscript.

Funding This research was funded by National Natural Science Foundation of China grant number 51875005.

Declarations

Conflict of interest The authors declare no competing interests.

References

1. Zheng Z, Jin X, Bai Y, Yang Y, Ni C, Lu WF, Wang H (2022) Microstructure and anisotropic mechanical properties of selective laser melted Ti6Al4V alloy under different scanning strategies. *Mater Sci Eng A Struct* 831:142236. <https://doi.org/10.1016/j.msea.2021.142236>
2. Yan X, Yin S, Chen C, Jenkins R, Lupoi R, Bolot R, Ma W, Kuang M, Liao H, Lu J, Liu M (2019) Fatigue strength improvement of selective laser melted Ti6Al4V using ultrasonic surface mechanical attrition. *Mater Res Lett* 7(8):327–333. <https://doi.org/10.1080/21663831.2019.1609110>
3. Shi C, Lu N, Qin Y, Liu M, Li H, Li H (2021) Study on mechanical properties and permeability of elliptical porous scaffold based on the SLM manufactured medical Ti6Al4V. *Plos One* 16(3):e0247764. <https://doi.org/10.1371/journal.pone.0247764>
4. Milton S, Rigo O, LeCorre S, Morandau A, Siriki R, Bocher P, Leroy R (2021) Microstructure effects on the machinability behaviour of Ti6Al4V produced by Selective Laser Melting and Electron Beam Melting process. *Mater Sci Eng A* 823:141773. <https://doi.org/10.1016/j.msea.2021.141773>
5. Xie B, Fan Y, Zhao S (2021) Characterization of Ti6Al4V powders produced by different methods for selective laser melting. *Mater Res Express* 8:76510. <https://doi.org/10.1088/2053-1591/ac10d1>
6. Palmeri D, Buffa G, Pollara G, Fratini L (2021) The effect of building direction on microstructure and microhardness during selective laser melting of Ti6Al4V titanium alloy. *J Mater Eng Perform* 30:8725–8734. <https://doi.org/10.1007/s11665-021-06039-x>
7. Bandyopadhyay A, Traxel KD (2018) Invited review article: metal-additive manufacturing—Modeling strategies for application-optimized designs. *Addit Manuf* 22:758–774. <https://doi.org/10.1016/j.addma.2018.06.024>
8. Mangat AS, Singh S, Gupta M, Sharma R (2018) Experimental investigations on natural fiber embedded additive manufacturing-based biodegradable structures for biomedical applications. *Rapid Prototyp J* 24:1221–1234. <https://doi.org/10.1108/RPJ-08-2017-0162>
9. Chen Z, Yan X, Yin S, Liu L, Liu X, Zhao G, Ma W, Qi W, Ren Z, Liao H, Liu M, Cai D, Fang H (2020) Influence of the pore size and porosity of selective laser melted Ti6Al4V ELI porous scaffold on cell proliferation, osteogenesis and bone ingrowth. *Mater Sci Eng C* 106:110289. <https://doi.org/10.1016/j.msec.2019.110289>
10. Vastola G, Zhang G, Pei QX, Zhang YW (2015) Modeling and control of remelting in high-energy beam additive manufacturing. *Addit Manuf* 7:57–63. <https://doi.org/10.1016/j.addma.2014.12.004>

11. Ahn IH (2019) Determination of a process window with consideration of effective layer thickness in SLM process. *Int J Adv Manuf Technol* 105:4181–4191. <https://doi.org/10.1007/s00170-019-04402-w>
12. Ma M, Wang Z, Gao M, Zeng X (2015) Layer thickness dependence of performance in high-power selective laser melting of 1Cr18Ni9Ti stainless steel. *J Mater Process Technol* 215:142–150. <https://doi.org/10.1016/j.jmatprotec.2014.07.034>
13. Wang S, Liu Y, Shi W, Qi B, Yang J, Zhang F, Han D, Ma Y (2017) Research on high layer thickness fabricated of 316L by selective laser melting. *Materials* 10(9):1055. <https://doi.org/10.3390/ma10091055>
14. Liu Y, Zhang M, Shi W, Ma Y, Yang J (2021) Study on performance optimization of 316L stainless steel parts by high-efficiency selective laser melting. *Opt Laser Technol* 138:106872. <https://doi.org/10.1016/j.optlastec.2020.106872>
15. Savalani MM, Pizarro JM (2016) Effect of preheat and layer thickness on selective laser melting (SLM) of magnesium. *Rapid Prototyp J* 22:115–122. <https://doi.org/10.1108/RPJ-07-2013-0076>
16. Di W, Yongqiang Y, Xubin S, Yonghua C (2012) Study on energy input and its influences on single-track, multi-track, and multi-layer in SLM. *Int J Adv Manuf Technol* 58:1189–1199. <https://doi.org/10.1007/s00170-011-3443-y>
17. Nguyen QB, Luu DN, Nai SML, Zhu Z, Chen Z, Wei J (2018) The role of powder layer thickness on the quality of SLM printed parts. *Arch Civ Mech Eng* 18:948–955. <https://doi.org/10.1016/j.acme.2018.01.015>
18. Greco S, Gutzeit K, Hotz H, Kirsch B, Aurich JC (2020) Selective laser melting (SLM) of AISI 316L—impact of laser power, layer thickness, and hatch spacing on roughness, density, and micro-hardness at constant input energy density. *Int J Adv Manuf Technol* 108:1551–1562. <https://doi.org/10.1007/s00170-020-05510-8>
19. Sufiarov VS, Popovich AA, Borisov EV, Polozov IA, Masaylo DV, Orlov AV (2017) The effect of layer thickness at selective laser melting. *Procedia Eng* 174:126–134. <https://doi.org/10.1016/j.proeng.2017.01.179>
20. Li F, Wang Z, Zeng X (2017) Microstructures and mechanical properties of Ti6Al4V alloy fabricated by multi-laser beam selective laser melting. *Mater Lett* 199:79–83. <https://doi.org/10.1016/j.matlet.2017.04.050>
21. de Formanoir C, Paggi U, Colebrants T, Thijs L, Li G, Vanmeensel K, Hooreweder BV (2020) Increasing the productivity of laser powder bed fusion: influence of the hull-bulk strategy on part quality, microstructure and mechanical performance of Ti-6Al-4V. *Addit Manuf* 33:101129. <https://doi.org/10.1016/j.addma.2020.101129>
22. Zhao R, Chen C, Wang W, Cao T, Shuai S, Xu S, Hu T, Liao H, Wang J, Ren Z (2022) On the role of volumetric energy density in the microstructure and mechanical properties of laser powder bed fusion Ti-6Al-4V alloy. *Addit Manuf* 51:102605. <https://doi.org/10.1016/j.addma.2022.102605>
23. Xu W, Lui EW, Pateras A, Qian M, Brandt M (2017) In situ tailoring microstructure in additively manufactured Ti-6Al-4V for superior mechanical performance. *Acta Mater* 125:390–400. <https://doi.org/10.1016/j.actamat.2016.12.027>
24. Shi W, Wang P, Liu Y, Hou Y, Han G (2020) Properties of 316L formed by a 400W power laser selective laser melting with 250μm layer thickness. *Powder Technol* 360:151–164. <https://doi.org/10.1016/j.powtec.2019.09.059>
25. Shi X, Yan C, Feng W, Zhang Y, Leng Z (2020) Effect of high layer thickness on surface quality and defect behavior of Ti-6Al-4V fabricated by selective laser melting. *Opt Laser Technol* 132:106471. <https://doi.org/10.1016/j.optlastec.2020.106471>
26. Milton S, Morandeanu A, Chalou F, Leroy R (2016) Influence of finish machining on the surface integrity of Ti6Al4V produced by selective laser melting. *Procedia CIRP* 45:127–130. <https://doi.org/10.1016/j.procir.2016.02.340>
27. Vaithilingam J, Prina E, Goodridge RD, Hague RJM, Edmondson S, Rose FRAJ, Christie SDR (2016) Surface chemistry of Ti6Al4V components fabricated using selective laser melting for biomedical applications. *Mater Sci Eng C* 67:294–303. <https://doi.org/10.1016/j.msec.2016.05.054>
28. Kelly CN, Evans NT, Irvin CW, Chapman SC, Gall K, Safranski DL (2019) The effect of surface topography and porosity on the tensile fatigue of 3D printed Ti-6Al-4V fabricated by selective laser melting. *Mater Sci Eng C* 98:726–736. <https://doi.org/10.1016/j.msec.2019.01.024>
29. King WE, Anderson AT, Ferencz RM, Hodge NE, Kamath C, Khairallah SA, Rubenchik AM (2015) Laser powder bed fusion additive manufacturing of metals; physics, computational, and materials challenges. *Appl Phys Rev* 2:41304. <https://doi.org/10.1063/1.4937809>
30. Gong H, Rafi K, Gu H, Starr T, Stucker B (2014) Analysis of defect generation in Ti-6Al-4V parts made using powder bed fusion additive manufacturing processes. *Addit Manuf* 1–4:87–98. <https://doi.org/10.1016/j.addma.2014.08.002>
31. Liu QC, Elambasseril J, Sun SJ, Leary M, Brandt M, Sharp PK (2014) The effect of manufacturing defects on the fatigue behaviour of Ti-6Al-4V specimens fabricated using selective laser melting. *AMR* 891–892:1519–1524. <https://doi.org/10.4028/www.scientific.net/amr.891-892.1519>
32. Zhao GY, Wang DD, Bai PK, Liu B (2010) Research progress of laser rapid prototyping technology for aluminum alloy. *Hot Work Technol* 39(9):170–173. <https://doi.org/10.3788/HPLPB2010208.1780.177>
33. Zhang B, Li Y, Bai Q (2017) Defect formation mechanisms in selective laser melting: a review. *Chin J Mech Eng* 30:515–527. <https://doi.org/10.1007/s10033-017-0121-5>
34. Xia M, Gu D, Yu G, Dai D, Chen H, Shi Q (2017) Porosity evolution and its thermodynamic mechanism of randomly packed powder-bed during selective laser melting of Inconel 718 alloy. *Int J Mach Tools Manuf* 116:96–106. <https://doi.org/10.1016/j.ijmactools.2017.01.005>
35. Körner C, Bauereiß A, Attar E (2013) Fundamental consolidation mechanisms during selective beam melting of powders. *Model Simul Mater Sci Eng* 21:85011. <https://doi.org/10.1088/0965-0393/21/8/085011>
36. Wang D, Wu S, Fu F, Mai S, Yang Y, Liu Y, Song C (2017) Mechanisms and characteristics of spatter generation in SLM processing and its effect on the properties. *Mater Des* 117:121–130. <https://doi.org/10.1016/j.matdes.2016.12.060>
37. Spierings AB, Herres N, Levy G (2011) Influence of the particle size distribution on surface quality and mechanical properties in AM steel parts. *Rapid Prototyp J* 17:195–202. <https://doi.org/10.1108/13552541111124770>
38. Vrancken B, Thijs L, Kruth J-P, Van Humbeek J (2012) Heat treatment of Ti6Al4V produced by selective laser melting: microstructure and mechanical properties. *J Alloys Compd* 541:177–185. <https://doi.org/10.1016/j.jallcom.2012.07.022>
39. Bartolomeu F, Faria S, Carvalho O, Pinto E, Alves N, Silva FS, Miranda G (2016) Predictive models for physical and mechanical properties of Ti6Al4V produced by Selective Laser Melting. *Mater Sci Eng A* 663:181–192. <https://doi.org/10.1016/j.msea.2016.03.113>
40. Burgers WG (1934) On the process of transition of the cubic-body-centered modification into the hexagonal-close-packed modification of zirconium. *Physica* 1:561–586. [https://doi.org/10.1016/S0031-8914\(34\)80244-3](https://doi.org/10.1016/S0031-8914(34)80244-3)
41. Zhang B, Liao H, Coddet C (2013) Microstructure evolution and density behavior of CP Ti parts elaborated by self-developed

- vacuum selective laser melting system. *Appl Surf Sci* 279:310–316. <https://doi.org/10.1016/j.apsusc.2013.04.090>
42. Broderick TF, Jackson AG, Jones H, Froes FH (1985) The effect of cooling conditions on the microstructure of rapidly solidified Ti-6Al-4V. *Metall Trans A* 16:1951–1959. <https://doi.org/10.1007/BF02662396>
 43. Yang J, Yu H, Yin J, Gao M, Wang Z, Zeng X (2016) Formation and control of martensite in Ti-6Al-4V alloy produced by selective laser melting. *Mater Des* 108:308–318. <https://doi.org/10.1016/j.matdes.2016.06.117>
 44. Han J, Yang J, Yu H, Yin J, Gao M, Wang Z, Zeng X (2017) Microstructure and mechanical property of selective laser melted Ti6Al4V dependence on laser energy density. *Rapid Prototyp J* 23:217–226. <https://doi.org/10.1108/RPJ-12-2015-0193>
 45. Kumar P, Ramamurty U (2019) Microstructural optimization through heat treatment for enhancing the fracture toughness and fatigue crack growth resistance of selective laser melted Ti6Al4V alloy. *Acta Mater* 169:45–59. <https://doi.org/10.1016/j.actamat.2019.03.003>
 46. Wei K, Li F, Huang G, Liu M, Deng J, He C, Zeng X (2021) Multi-laser powder bed fusion of Ti-6Al-4V alloy: defect, microstructure, and mechanical property of overlap region. *Mater Sci Eng A* 802:140644. <https://doi.org/10.1016/j.msea.2020.140644>
 47. Flower HM (1990) Microstructural development in relation to hot working of titanium alloys. *Mater Sci Technol* 6:1082–1092. <https://doi.org/10.1179/mst.1990.6.11.1082>
 48. Wu X, Liang J, Mei J, Mitchell C, Goodwin PS, Voice W (2004) Microstructures of laser-deposited Ti-6Al-4V. *Mater Des* 25:137–144. <https://doi.org/10.1016/j.matdes.2003.09.009>
 49. Yang J, Yu H, Wang Z, Zeng X (2017) Effect of crystallographic orientation on mechanical anisotropy of selective laser melted Ti-6Al-4V alloy. *Mater Charact* 127:137–145. <https://doi.org/10.1016/j.matchar.2017.01.014>
 50. Kobryn PA, Semiatin SL (2001) Mechanical properties of laser-deposited Ti-6Al-4V. 2001 International Solid Freeform Fabrication Symposium. The University of Texas at Austin, Austin, TX, USA 179–186. <https://doi.org/10.26153/tsw/3261>
 51. Yu H, Yang J, Yin J, Wang Z, Zeng X (2017) Comparison on mechanical anisotropies of selective laser melted Ti-6Al-4V alloy and 304 stainless steel. *Mater Sci Eng A* 695:92–100. <https://doi.org/10.1016/j.msea.2017.04.031>
 52. Carroll BE, Palmer TA, Beese AM (2015) Anisotropic tensile behavior of Ti-6Al-4V components fabricated with directed energy deposition additive manufacturing. *Acta Mater* 87:309–320. <https://doi.org/10.1016/j.actamat.2014.12.054>
 53. Wang P, Chen D, Fan J, Sun K, Wu S, Li J, Sun Y (2022) Study on the influence of process parameters on high performance Ti-6Al-4V parts in laser powder bed fusion. *Rapid Prototyp J* 28:1655–1676. <https://doi.org/10.1108/RPJ-09-2021-0235>
 54. Simonelli M, Tse YY, Tuck C (2012) Further understanding on Ti-6Al-4V selective laser melting using texture analysis. *J Phys Confer Ser* 371:1–4
 55. Shi X, Ma S, Liu C, Chen C, Wu Q, Chen X, Lu J (2016) Performance of high layer thickness in selective laser melting of Ti6Al4V. *Mater* 9(12):975. <https://doi.org/10.3390/ma9120975>

Publisher's note Springer Nature remains neutral with regard to jurisdictional claims in published maps and institutional affiliations.

Springer Nature or its licensor (e.g. a society or other partner) holds exclusive rights to this article under a publishing agreement with the author(s) or other rightsholder(s); author self-archiving of the accepted manuscript version of this article is solely governed by the terms of such publishing agreement and applicable law.